Materials Advances

ROYAL SOCIETY OF CHEMISTRY

PAPER

View Article Online
View Journal | View Issue

Check for updates

Cite this: *Mater. Adv.*, 2022, 3, 3980

Phase engineered gallium ferrite: a promising narrow bandgap, room-temperature ferroelectric†

Somdutta Mukherjee,*[a] Monali Mishra,[ab] Palash Swarnakar,[c] Shilpa Sanwlani,[d] Sukalyan Dash[b] and Amritendu Roy*[c]

Received 25th January 2022,
Accepted 24th March 2022

DOI: 10.1039/d2ma00089j

rsc.li/materials-advances

Narrow bandgap oxide ferroelectrics with large polarization are considered promising in novel optoelectronic and photovoltaic devices. In the present work, nanocrystalline gallium ferrite with polar, rhombohedral *R3c* symmetry is synthesized using the hydrothermal route. Structural characterization using X-ray diffraction, Raman spectroscopy, and electron microscopy confirm the formation of the rhombohedral *R3c* phase, with two different geometries and narrow size distribution. Electrical characterization corroborated by first-principles density functional theory-based calculations demonstrates room temperature ferroelectricity contributed mainly by triply charged gallium ions. The calculated spontaneous polarization is ~20 μC cm^{-2} with a large electronic contribution. Optical characterization predicts a bandgap of ~2.1 eV. Together with its narrow bandgap and the large contribution of electronic polarization, ferroelectric gallium ferrite could be an interesting system for novel photovoltaic and optoelectronic devices.

1. Introduction

Ferroelectric (FE) materials continue to present challenging physics as well as exciting technological applications in diverse, novel electronic devices including solid-state non-volatile memory elements, field-effect transistors and micro- and nano-electromechanical systems such as sensors, actuators, and transducers.[1,2] More recently, FEs have been considered promising for visible light photovoltaic applications wherein spontaneous polarization is presumed to be instrumental for the separation of photogenerated charge carriers. In this regard, halide perovskites[3–5] with their favourable optoelectronic characteristics have yielded impressive conversion efficiencies. Perovskite halides, however, suffer from poor stability and potential environmental impacts.[6] While improvement towards their stability has been a major research focus,[6] the design and development of stable, environment-friendly materials demonstrating an enhanced PV effect could constitute an important avenue in solar cell research.

In this context, transition metal oxide (TMOs) based perovskite ferroelectrics render wide opportunities towards tailoring desired functionalities owing to their competing energy scales of various phases and susceptibility to external perturbations.[7] However, traditional TMO ferroelectrics demonstrate a large optical bandgap resulting in poor absorption behaviour in the visible part of the solar spectra and therefore yields very small photocurrent vis-à-vis conversion efficiency.[8] Thus, tailoring the bandgap is the first step towards designing efficient solar cell materials based on these materials. While selective doping,[9–11] solid solution formations[8,12] and gap-state engineering[13] have been explored to reduce the bandgap of traditional TMO-ferroelectrics, single-phase ferroelectric-multiferroics with a comparatively low bandgap, are superior choices.[14]

Transition metal oxide ferroelectric-multiferroic bismuth ferrite ($BiFeO_3$ or BFO) is a classic example of a room-temperature multiferroic material with rhombohedral symmetry.[15] BFO with a large spontaneous polarization and bandgap of ~2.7 eV has been shown to possess good PV performance.[16,17] However, the bandgap in BFO is far from the ideal value of ~1.4 eV for efficient absorption of solar radiation. Therefore, it would be desirable to design novel room temperature ferroelectric/multiferroic systems with a narrow bandgap for prospective solar cell applications.

More recently, gallium ferrite ($GaFeO_3$ or GFO) has come up as an alternative room temperature MF with sizable spontaneous polarization and room temperature ferrimagnetism.[10,18] Bulk GFO with orthorhombic $Pna2_1$ symmetry demonstrates cation site-disorder as well as a wide range of cationic non-stoichiometry which in turn, translates to tunable magnetic vis-à-vis multiferroic transition temperature.[19] Nanoscale piezo-response force measurements on epitaxial[10] as well as solution

[a] *Materials Chemistry Department, CSIR-IMMT Bhubaneswar, Bhubaneswar, 751013, Orissa, India. E-mail: msomdutta@gmail.com*
[b] *Department of Chemistry, VSSUT Burla, Burla, 768018, India*
[c] *School of Minerals, Metallurgical and Materials Engineering, Indian Institute of Technology Bhubaneswar, Jatni, 752050, Orissa, India. E-mail: amritendu@iitbbs.ac.in*
[d] *Department of Physics, Indian Institute of Science, Education and Research Mohali, Punjab, India*

† Electronic supplementary information (ESI) available. See https://doi.org/10.1039/d2ma00089j

deposited[18] films demonstrated 180° phase switching upon changing the bias field. Bulk measurement on epitaxially grown films further showed a saturated ferroelectric hysteresis loop.[20] The observed poor leakage characteristics could be effectively improved by selective doping.[21] As such, GFO is quickly emerging as an effective substitute for BFO. Despite the above attributes, the required electric field for switching the ferroelectric domains in bulk GFO was found to be rather high, ~1400 kV cm^{-1}.[10,20] Thus, to use GFO for commercial device applications, the coercive field of GFO needs to be reduced substantially. In this regard, the possibility of stabilizing a novel ferroelectric phase of the system with a smaller bandgap and coercive field seems exciting from device designing perspectives. GFO has been shown to undergo a series of structural phase transformations across a wide range of hydrostatic pressure.[22] Among the observed high-pressure phases,[22] a few are polar and keep the promise to demonstrate ferroelectricity. Thus, it would be interesting to explore the feasibility of synthesizing vis-à-vis stabilizing such high-pressure phases at ambient conditions upon applying suitable processing conditions and evaluate their properties for possible room-temperature ferroelectricity/multiferroism. In a recent work, the present authors synthesized GFO nanocrystals with unique truncated hexagonal bi-pyramid (THBP) geometry using a hydrothermal technique.[23] Subsequent structural and functional characterization demonstrated an orthorhombic $P2_12_12_1$ symmetry with a moderately small bandgap and exciting photocatalytic activity.[23]

In the present work, we stabilize GFO nanocrystals with rhombohedral *R3c* symmetry at room-temperature. Electrical, magnetic and optical characterization together with first-principles studies establish the material as a room-temperature ferroelectric with a reduced coercive field and narrow optical band gap (~2.1 eV). Electrical characterization further demonstrates rectifying characteristics. Phase engineered GFO thus possesses promise for novel optoelectronic and photovoltaic applications and demands further investigations.

2. Experimental and computational details

2.1 Experiments

THBP GFO nanocrystals were synthesized using a hydrothermal method following a protocol as reported earlier by the present authors.[23] Gallium nitrate hydrate ($Ga(NO_3)_3{\cdot}xH_2O$) (Sigma Aldrich ≥99.9%) and iron nitrate nonahydrate ($Fe(NO_3)_3{\cdot}9H_2O$) (Sigma Aldrich ≥98%) were taken in stoichiometric ratio and dissolved in 40 ml deionized water (pH = 6.8). The concentration of precursors in the solution was four times in the case of protocol (ii) in comparison to that of protocol (i). No reducing or shape defining reagent was used. The solution was transferred to a Teflon liner and autoclaved at 523 K for 5 h. In order to obtain the required phase, the as-grown powder was heated for 1 h at 673 K. We would henceforth call this synthesis route protocol (i). However, the yield of the above process is too low to effectively use it for extensive characterization. It was further observed that the required phase could also be stabilized when the amount of precursors was increased to four times keeping other processing parameters identical to our earlier work,[23] *viz.*, 523 K and 5 h (protocol (ii)).

The morphology of the as prepared samples was examined using a field emission scanning electron microscope (FESEM) (Zeiss, Merlin Compact) and a transmission electron microscope. Powder X-ray diffraction patterns of the synthesized crystals were acquired over the 2θ range 10–90° using a Bruker D8 Advance diffractometer with CuKα radiation (λ = 1.5418 Å). Rietveld refinement of the room temperature powder X-ray diffraction data was carried out using FullProf[24] with two different space groups, *viz.*, *R3c* and $R\bar{3}c$. Thermal analysis (DSC) was carried out using a Differential scanning calorimeter (METTLER TOLEDO). To study the optical properties, ultraviolet-visible (UV-vis) (Shimadzu-UV-2450, Japan) spectra was recorded using a non-absorbing standard $BaSO_4$ powder. An impedance spectroscopy study was conducted in a WayneKerr 6505 B impedance analyser. The bulk ferroelectric hysteresis loop was measured in a Radiant Precision Premier II ferroelectric tester. Piezoresponse force microscopy using the switching spectroscopy mode (Asylum) was performed to study the local response.

2.2 Computation

First-principles calculations were carried out using density functional theory[25] as implemented in Vienna *Ab initio* Simulation Package (VASP)[26,27] using the generalized gradient approximation (GGA)[28] as well as with suitable application of onsite Coulomb potential (GGA+U with U_{eff} = 2.0 to 4.0 eV)[29,30] to treat the strongly correlated 3d-electrons of Fe ions. We used a rotationally invariant approach[31] for U_{eff}, the magnitude of which was determined based on our previous experience on the material. The Kohn–Sham equation[32] was solved using the Perdew and Wang (PW91) functional.[33] A large kinetic energy cut-off of the planewaves, 850 eV, was used. Our entire calculations are based on the stoichiometric composition of $GaFeO_3$ with the assumption that no partial interchange of the lattice sites by constituent cations have taken place. We included thirteen valence electrons for Ga ($3d^{10}4s^24p^1$), eight for Fe ($3d^74s^1$) and six for O ($2s^22p^4$) ions. We used conjugate gradient algorithm for relaxing the constituent ions within a unit cell constructed using the data obtained from Rietveld refinement of the XRD pattern at room temperature (Table 1). All the calculations were performed at 0 K. Calculation of the electronic structure was carried out using an 8 × 8 × 3 Gamma (Γ-) mesh. Polarization was computed using the Berry phase method within modern theory of polarization.[34]

3. Results and discussion

3.1 Structural and microstructural characterization

3.1.1 Powder X-ray diffraction study. Differential scanning calorimetry (DSC) together with temperature-dependent powder X-ray diffraction studies (refer to the ESI,† S.1a and S.1b) of the as-synthesized sample from our previous work, predict a prominent

Table 1 Refined structural parameters of Rhombohedral *R3c* gallium ferrite obtained from Rietveld refinement of the powder X-ray diffraction of the sample synthesized using protocol (ii). Conventional Rietveld parameters are: R_p = 32.1; R_{wp} = 12.9 and R_{exp} = 10.6

Phase: $R\bar{3}c$ (SG#161)				
Lattice parameters: $a = b = 5.0235$ Å; $c = 13.6325$ Å; $\alpha = \beta = 90^\circ$; $\gamma = 120^\circ$				
Ion	Wyckoff positions	x	Y	z
Ga^{3+}	6a	0.0000	0.0000	0.3075
Fe^{3+}	6a	0.0000	0.0000	0.0186
O^{2-}	18b	−0.3005	−0.2988	0.4062

phase transformation across ~650–673 K where at room temperature, the orthorhombic $P2_12_12_1$ phase[23] transforms to a higher symmetry (fewer peaks) phase. An initial evaluation of the XRD data indicated rhombohedral symmetry. It was also observed that the above orthorhombic to rhombohedral transformation is irreversible and annealing of the room temperature phase at 673 K for 1 h retains the rhombohedral symmetry. However, the yield of the above processing protocol is too small to further characterize the sample, especially for bulk electrical measurement. Thus, we needed a different synthesis protocol that would give rise to the same rhombohedral crystal symmetry with greater yield. Consequent trials revealed that when the ratio of the precursor was increased four times with respect to the previous protocol, keeping the temperature, time, and volume of the hydrothermal cell during synthesis identical *i.e.*, 523 K and 5 h, we ended up getting the identical XRD pattern to that of the sample annealed at 673 K, this time, at room temperature. Subsequent studies were made on samples both processed without annealing (protocol ii) with the precursor concentration increased to four times as well as on the sample prepared earlier and then annealed at 673 K for 1 h (protocol i).

The room temperature powder XRD pattern of the as-synthesized sample prepared using the modified protocol (protocol – ii) is shown in Fig. 1(a). Rietveld refinement of the powder pattern was attempted using two rhombohedral symmetries, *viz.*, polar *R3c* (Space Group #161) and non-polar $R\bar{3}c$ (Space Group # 167). It is not practically possible to differentiate between the above two phases which belong to the same Laue groups, based on powder X-ray diffraction data. However, it is observed that polar *R3c* (with refined atom positions, 0 0 δ ($\delta \neq \frac{1}{4}$)) yields a much better goodness of fit in comparison to that of 0 0 $\frac{1}{4}$ corresponding to non-polar $R\bar{3}c$. Accordingly, the symmetry of the phase of the sample is assigned as *R3c*. Structural parameters obtained from the refinement as well as the refinement parameters are presented in Table 1. Fig. 1(b) schematically depicts the unit cell of *R3c*-GFO in the hexagonal setting. Our subsequent first-principles study, in section 3.6 and electrical characterization, in section 3.5, further bolster the stability of the *R3c* symmetry of the material over $R\bar{3}c$ and thus, corroborate the powder XRD analysis.

3.1.2 Raman study. *R3c* symmetry of GFO nanocrystals synthesized through both the protocol (i) and (ii) is further supported using room temperature Raman spectra analysis

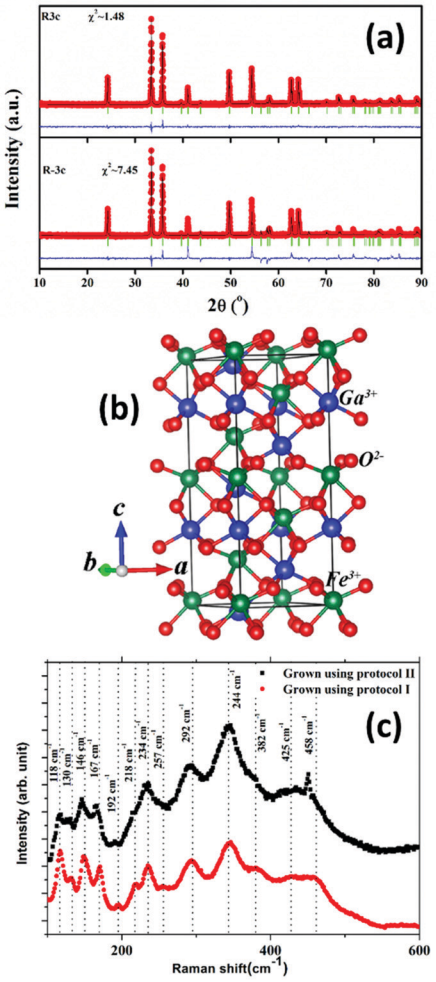

Fig. 1 (a) Rietveld refinement of the room temperature XRD pattern of the gallium ferrite (GFO) nanocrystal sample prepared by protocol (ii), using *R3c* and $R\bar{3}c$ symmetries. (b) Schematic description of the unit cell of GFO with *R3c* symmetry. (c) Raman spectra of *R3c*-GFO synthesized using the two different protocols.

probed using the Ar^+ laser of 514 nm as an excitation source. Fig. 1(c) shows the Raman spectra of both the crystals over 100–600 cm^{-1}.

The polar *R3c* phase with space group #161 is comprised of 30 atoms or 6 formula units within the rhombohedral unit cell in the hexagonal setting. Following group theory, the irreducible representation that presents the Raman active modes at the zone-center is Γ = 4A1 + 9E *i.e.* a total of 13 modes are expected. As can be seen from Fig. 1(c), 13 distinct Raman peaks are identified over the frequency range 100–600 cm^{-1} for both the *R3c* GFO nanocrystals grown using protocol (i) as well as protocol (ii). A comparison of the peak positions with those of *R3c*-BFO suggests modes between 152–261 cm^{-1} involve the Fe–O bending and stretching of bonds within FeO_6 octahedra, while oxygen motions dominate above 261 cm^{-1}.[35] Raman modes related to Ga–O bonds are expected to appear below ~170 cm^{-1} though a blue shift of mode positions is expected due to the lower reduced mass of Ga–O compared to Bi–O.[35]

3.1.3 Microstructural studies: scanning and transmission electron microscopy. Field emission scanning electron micrographs of the samples prepared through protocol (i) and (ii) are shown in Fig. 2(a and b). It is observed that the morphology of the sample prepared by protocol (i) remains truncated hexagonal bi-pyramidal (THBP) while protocol (ii) yielded cuboidal shaped nanoparticles. Average axial lengths of the nanocrystals produced in the two routes are ~150 nm and ~200 nm, respectively, for protocol (i) and (ii). Since the time and temperature of the two hydrothermal processing conditions are similar, the observed variation in the size and geometry of the nanostructure could originate from the variation in the supersaturation arising due to different precursor concentrations in the solution from which the crystals are grown. A similar effect of supersaturation to determine the geometry and dimension was observed in previous studies on systems such as CdSe,[36] TiO2[37] and $SmVO_4$.[38] Elemental analysis using energy dispersive X-ray spectroscopy (EDAX) predicts that in either of the two cases the samples are Fe-rich, Ga: Fe = 0.78 ± 0.03 for protocol (i) and 0.64 ± 0.04 for protocol (ii), respectively, only predicting that some of the Ga sites have been taken by similar sized Fe ions in addition to the possible cation site disorder inherent to the system.

Transmission electron microscopy studies conducted on both the samples are shown in Fig. 2(c and d). Fig. 2(c) inset shows a single GFO nanocrystal prepared using protocol (i) demonstrating THBP geometry. High resolution TEM imaging of the nanocrystals (Fig. 2(c)) demonstrates atomic arrangements within parallel lattice planes without significant disruption in the periodic arrangement suggesting formation of defect free nanocrystals. Using the Rietveld data, we calculated interplaner spacing of several high index planes within *R*3*c* symmetry.

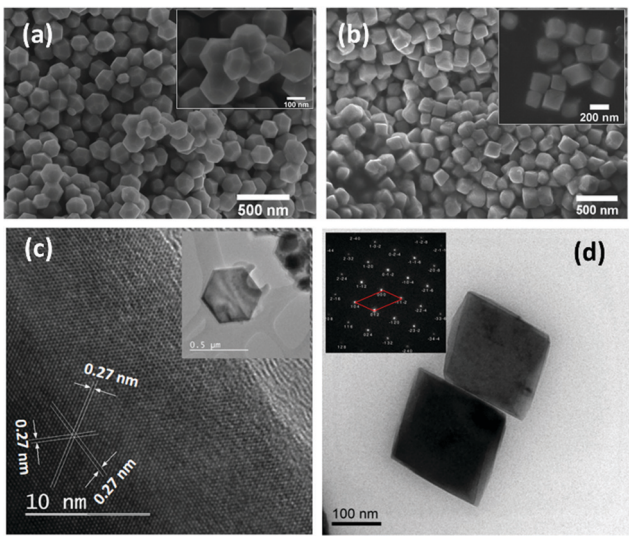

Fig. 2 Field emission scanning electron micrographs (FESEM) of the GFO nanocrystals synthesized using (a) protocol (i), and (b) protocol ii. The insets show the high magnification images. (c) High resolution transmission electron micrograph a GFO nanocrystal produced using protocol (i). The inset shows a single GFO nanocrystal. (d) TEM micrograph of the GFO sample synthesized using protocol (ii). The inset shows the diffraction pattern obtained from a single nanocrystal.

The measured interplaner spacing from the HRTEM images substantiates the presence of (104) planes. Fig. 2(d) presents the TEM image of samples prepared using protocol (ii). While the edges of the samples were too thick to produce any lattice images, the diffraction pattern (inset, Fig. 2(d)) predicts rhombohedral symmetry with lattice parameters similar to those predicted by Rietveld refinement, discussed above.

3.2 Mechanism of formation of GFO nanocrystals with varied crystal symmetry and shape

The mechanism of oxide nanostructure evolution during hydrothermal synthesis is explained in light of the kinetics and thermodynamics of the processing, that provide complementary descriptions. The critical balance between the two, determines the crystal symmetry, size and shape of the synthesized nanocrystalline phase. In the present work, we observe that GFO nanocrystals are formed with two different crystal symmetries, *viz.*, $P2_12_12_1$ and *R*3*c* and geometries, *i.e.*, truncated hexagonal bipyramid (THBP) and cubic geometries under protocol (i) (without annealing)[23] and (ii), respectively, described in section 2. In either of the two processes, no capping agent was used and the synthesized nanoparticles are of fairly uniform size.

The evolution of the GFO nanostructure begins with the progress of the monomer forming reaction under thermal activation:[23] $Ga(NO_3)_3 + Fe(NO_3)_3 + 3H_2O = GaFeO_3 + 6HNO_3$ With time elapsed, monomer concentration in the solution increases rapidly. Beyond the critical supersaturation level, nucleation (self-nucleation) starts. The process of nucleation involves crossing the activation energy barrier by a monomer from the bulk of the solution to a growing nucleus. A smaller activation barrier would favour nucleation of a particular crystalline phase. The driving force for crystallization is the change in chemical potential ($\Delta\mu$) while the monomer travels from the dissolved phase to the solid crystalline phase:

$$\Delta\mu = \mu_S - \mu_L + -kT\ln S \quad (1)$$

where μ_S and μ_L represent chemical potentials in the crystalline solid and solution phases, respectively, and S denotes supersaturation given by the ratio of the monomer concentration in the solution (C) to the equilibrium monomer concentration within the crystalline phase (C_0). The associated bulk free energy change could be written as,

$$\Delta G_V = -\frac{RT}{V_m}\ln S = -\frac{RT}{V_m}\ln\frac{C}{C_0} \quad (2)$$

where V_m is the molar volume of the monomers within the crystalline phase and R is the universal gas constant. With the available data, we observe that the supersaturation in the two protocols differs by ~400% and that the ΔG_V value for the *R*3*c* phase is ~25% smaller in protocol (ii).

Assuming homogenous nucleation, for a critical sized, spherical nucleus of radius r, the net change in free energy can be expressed as the sum of bulk and surface contributions:[39]

$$\Delta G_N = \frac{4}{3}\pi r^3\Delta G_V + 4\pi r^2\gamma = \frac{16\pi\gamma^3 V_m^2}{3k^3T^3N_A^2(\ln S)^2} \quad (3)$$

where, γ represents the surface free energy associated with the formation of a nucleus with particular crystal symmetry and can be approximated as, γ = Ka; where K is defined as the so-called cohessional pressure and a is the average distance between lattice layers approximated as, $a = \left(\frac{V_m}{N_A}\right)^{1/3}$.[40] Thus, for a qualitative study, γ could be described as:

$$\gamma = K\left(\frac{V_m}{N_A}\right)^{1/3} \quad (4)$$

Here, N_A is Avogadro's number. With the above substitution, the expression for ΔG_N becomes:

$$\Delta G_N = \frac{16\pi K^3 V_m^3}{3k^3 T^3 N_A^3 (\ln S)^2} \quad (5)$$

where k, T, and N_A represent Boltzmann constant, reaction temperature in absolute scale, and Avogadro's number, respectively and ΔG_N can be interpreted as the free energy change associated with the nucleation process while the monomer crosses the activation barrier from the solution phase to the nucleus. Eqn (5) suggests that a small molar volume and large supersaturation would result in small ΔG_N. Crystallographic information obtained from our present study and previous work[23] show that the *R*3*c* phase possesses ~14% higher molar volume in comparison to the $P2_12_12_1$ phase. However, a ~400% increase in the monomer concentration in the solution would result in lowering of ΔG_N for *R*3*c* phase formation over $P2_12_12_1$ which albeit has a favourable molar volume, grew only when the supersaturation level in the solution was low. The nucleation rate could be written as:[39]

$$\frac{dN}{dt} = A\exp\left(-\frac{\Delta G_N}{kT}\right) = A\exp\left(-\frac{16\pi\gamma^3 V_m^2}{3k^3 T^3 N_A^2 (\ln S)^2}\right) \quad (6)$$

where N represents the number of nuclei at time, t; pre-exponent term, A is the jump frequency across the interface between the nucleus and bulk solution; a large value of S would translate rapid nucleation. The above expression further suggests that uniform size distribution of the nanocrystals, which is observed in our FESEM studies, would require burst nucleation where due to fast kinetics of the monomer forming reaction, the monomer concentration in the solution quickly increased which is followed by a large number of nucleation happening over a very short duration of time. When the chemical potential of the nuclei is high, any further nucleation is less favoured. On the contrary, more and more monomers are attached to the nuclei rendering them critical-sized. Following this, the critical-sized nuclei grow at the expense of monomer concentration within the solution.[39]

Our earlier study suggests that GFO nuclei formed within the solution demonstrate a shift from isotropic growth at lower temperature to THBP geometry at 250 °C suggesting a kinetics driven growth mechanism.[23] For achieving uniform size distribution of the particles, the growth should be diffusion-limited. However, it should be noted that there are no straightforward guidelines to predict the morphology of the particle since there are a number of factors that affect the morphology of the growing particle. The equilibrium shape (Gibbs–Wulff theory) of a particle is one that minimizes the surface energy for a given enclosed volume.[41] The isotropic surface energy would therefore result in spherical particles. A low monomer concentration in the solution further promotes spherical particle formation. A high monomer concentration on the other hand, favours anisotropic growth along directions with a lower activation energy barrier. The diffusion controlled growth model proposed by Peng[42] has been highly successful in explaining the shape variation of inorganic nanoparticles with varied monomer concentrations in the solution and can be used here. In the present work, under an identical temperature, the shape of the crystal changes to cubic when the precursor concentration in the solution is changed to four times. Apparently, the above modification is due to a change in supersaturation level during the synthesis process. It is believed that the supersaturation level influences the chemical potential in the bulk solution as well as the oriented attachment of the monomers.[38] In dilute solution, the system can reach a dynamic equilibrium by dissolution and regrowth of various facets with varied energies, resulting in the formation of nanospheres. A moderate supersaturation, on the other hand, results in directional growth. Variation in the chemical potential among the facets with different crystallographic orientation favours preferential migration of the monomers resulting in shapes such as THBP in intermediate monomer concentration and cubic in high monomer concentration. Similar supersaturation-driven shape evolution has been previously reported in TiO_2[37] and $SmVO_4$[38] where spherical shaped nanospheres are formed at a low monomer concentration while very high concentration promotes nanowire formation.

3.3 Optical property

Fig. 3(a) inset shows the optical absorption spectra of the *R*3*c*-GFO nanocrystal over the range 400–700 nm. It shows strong absorption in the wavelength range of 550–700 nm suggesting that the GFO nanocrystal can absorb a considerable amount of visible light. The absorption edge at ~600 nm can be attributed to $6A_{1g} \rightarrow 4T_{2g}$ (~2.0 ev) transition originating from the crystal field splitting of FeO_6 octahedra.[43] The optical band gap of the THBP-GFO nanocrystals was estimated using Tauc relation:[44] $(h\nu\alpha)^{1/n} = B(h\nu - E_g)$, where '$h$' is Planck's constant ($6.626 \times 10^{-34}$ m^2 kg s^{-1}), ν, represents the frequency of incident light, α, absorption coefficient, B, proportionality constant and E_g is the bandgap of the material. The value of the exponent n denotes the nature of the optical transition. For direct optical transition, $n = \frac{1}{2}$ while n = 2 represents indirect transition from the valence to conduction bands. Since the material was found to behave as a direct bandgap semiconductor, as shown in the following DFT study, a straight line fit on the linear part of $(\alpha h\upsilon)^2$ *vs.* $h\upsilon$ plot (Fig. 3(a)) was made to determine the bandgap of the material. The bandgap, estimated from the x-axis intercept is found to be ~2.1 eV. The observed bandgap is smaller than that in the bulk phase as well as significantly lower than that of BFO. This narrow bandgap renders the material to absorb a significantly large part of the solar spectrum and thereby promises an improved photocurrent response.

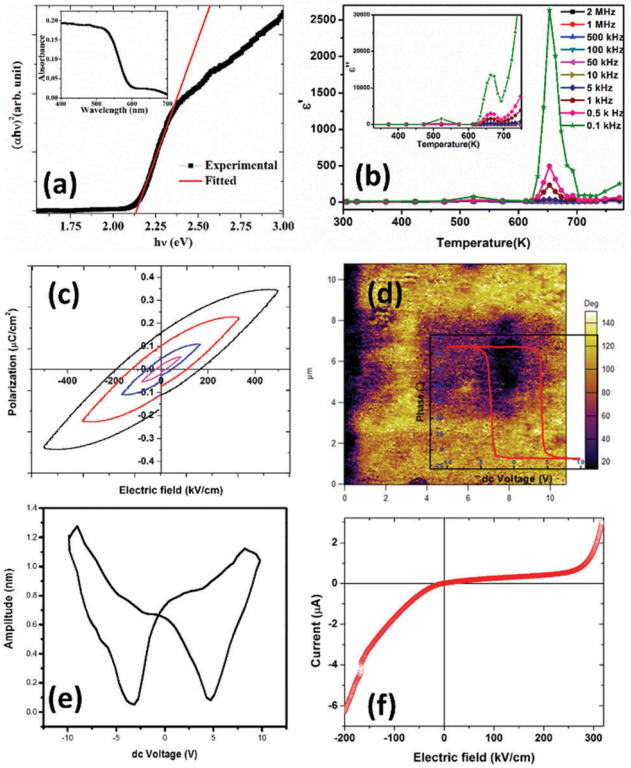

Fig. 3 (a) Tauc plot of optical absorption data demonstrating an optical band gap. The inset shows the absorption spectra of the *R*3*c* phase of GFO nanocrystals. (b) Real part of the dielectric constant (ε') *versus* temperature at certain frequencies; the inset plots the imaginary component dielectric constant (ε'') *versus* temperature at different frequencies within *R*3*c*-GFO. (c) Bulk polarization hysteresis data plotted as a function of applied voltage on a ~600 μm thick film of GFO on an ITO coated glass substrate. (d) PFM phase and (e) butterfly loop of GFO on ITO at room temperature. (f) Room temperature current–voltage plot on GFO thick-film on an ITO coated glass substrate demonstrating rectifying characteristics.

3.4 Electrical characterization

Temperature dependent impedance measurement of the sample, prepared using protocol (ii), was performed over a frequency range, 100 Hz–2 MHz. A similar exercise was conducted on the sample synthesized using protocol (i) and subsequent analysis is presented in the ESI.† The two data are identical. Using the impedance data, we calculated the real and imaginary part of the dielectric constant by using the following equation:

$$\varepsilon' = \frac{Z''}{\omega \times C_0 \times Z^2} \text{ and } \varepsilon'' = \frac{Z'}{\omega \times C_0 \times Z^2} \quad (7)$$

The real part of the dielectric constant (ε') for different frequency values are plotted as a function of temperature, as shown in Fig. 3(b). Z' and Z'' are real and imaginary parts of complex impedance Z; $\omega = 2\pi f$ where f is the measured frequency and C_0 is free space capacitance. It is observed that the present *R*3*c* phase possesses a high frequency dielectric constant, ε ~7 which is significantly smaller than traditional ferroelectrics such as $BaTiO_3$ over the temperature range, 300–600 K. The magnitude of the high frequency dielectric constant increases to maximum ~49 at the highest temperature used, 750 K. The dielectric constant depends upon different types of polarizations, *i.e.*, interfacial, dipolar, ionic and electronic polarization with increasing frequencies. While interfacial polarizations operate at lower frequencies, at high frequency, only dipolar (orientational), ionic and electronic polarizations are responsible. The constant magnitude over the entire range of temperature and frequency indicates that the observed dielectric constant is intrinsic in nature without interfacial contributions. As the temperature increased both ε' as well as ε'' exhibit anomalies at ~523 K and 653 K. The anomalies are prominent at lower frequencies as the ε' reaches maximum values 78 and 2633 at 523 and 653 K, respectively at 100 Hz. Temperature anomalies of ε' and ε'' are suggestive of structural phase transitions over the temperature window. This structural phase transformation is characteristic of ferroelectric materials where symmetry increasing structural transition translates to dielectric anomaly.

P *vs.* E plots demonstrate hysteresis behaviour. With increasing applied field (E), the size of the loop increases. The shape of the loop is typical of lossy ferroelectrics.[45] Early works on BFO[46] and GFO[47] report similar ferroelectric hysteresis loops. In fact, our DC current–voltage data on the sample demonstrates the presence of a large leakage current in the sample possibly hindering the true ferroelectric nature of the sample. Inappropriate sample preparation (sintering at high temperature could not be performed to avoid possible irreversible phase transformation) could be one of the origins of poor data.

The presence of multivalent Fe-ions could also contribute to increased leakage. However, with this nature of unsaturated ferroelectric hysteresis characteristics, one cannot conclusively confirm the presence of ferroelectricity in the sample. In order to further probe the possible ferroelectric character in the material and to minimize the effect of sample quality on the prospective ferroelectric property, local measurement using piezo-response force microscopy was conducted on the sample. In piezoresponse force microscopy, a 10 μm × 10 μm area of the sample was subjected to a positive bias, allowing all the domains to align unidirectionally. After that a 2 μm × 2 μm area within the poled sample was applied to a reverse bias, making the domains align in opposite directions. The phase image together with switching spectroscopy is presented in Fig. 3(d). The switching spectroscopy data and the phase image of the PFM study demonstrate 180° phase switching upon swapping the electric field direction. The corresponding amplitude plot (Fig. 3(e)) allows the piezoelectric co-efficient to be determined. The piezoelectric coefficient is derived using $d_{33} = \frac{A(bt)}{V_{ac} \times G}$, where $A(bt)$ is the change in thickness or deformation (amplitude of butterfly loop) and V_{ac} is the AC voltage given to the cantilever to apply an electric field. G is directly related to the quality factor of tuning of the cantilever, $G = \frac{A(F \pm 5kHz) \times Q_{factor}}{A(\text{peak})}$. The calculated piezoelectric coefficient was found to be d_{33} ~11 pm V^{-1}. The d_{33} value is comparable to the value reported for the epitaxial thin film of BFO[48] and other similar piezoelectric materials. For prospective

photovoltaic applications, it is important that GFO demonstrates rectifying characteristics, since this behaviour allows charge carriers of opposite polarities to separate out. In order to characterize the current–voltage behaviour of the material, a thick film (thickness, ~600 μm) of GFO on an ITO coated glass substrate was prepared. As shown in Fig. 3(f), with forward bias the current is very small and remains almost parallel to the voltage axis before, and it suddenly shoots up at a voltage of ~160 V. In the reverse bias, however, the current demonstrates a gradual increase with field. The above behaviour is similar to that of a diode which is required for separation of the photo-excited charge carriers. It is therefore observed that phase engineered GFO demonstrates a rectifying character, important for its potential PV application.

3.5 First-principles studies

First-principles calculations were performed within the framework of density functional theory.[49] We started with the structural information obtained from the Rietveld refinement of the room temperature X-ray diffraction pattern of the sample prepared using protocol (ii). The ionic positions were relaxed at the experimental cell volume until the force on individual ions became less than 0.0005 eV $Å^{-1}$. To determine the possible magnetic order, spin-polarized calculations within ferro- and antiferro-magnetic spin configurations of the Fe^{3+} ions were performed. It was found that anti-ferromagnetic orderings of the Fe-spins corresponds to 71 meV per atom lower in energy than ferromagnetic ordering within *R3c* symmetry of GFO. To probe further and therefore to determine possible antiferromagnetic ordering, a 2 × 2 × 1 supercell was constructed. The total energy of the 2 × 2 × 1 supercell was computed by enforcing different antiferromagnetic orders of the Fe^{3+}-ions, *viz.*, A-, C- and G-type antiferromagnetic orders. It was observed that the G-type antiferromagnetic order of the Fe^{3+} ions corresponds to the lowest energy, 23 meV per atom and 44 meV per atom lower with reference to C-AFM and A-AFM orderings, respectively. Thus, one can predict that stoichiometric GFO within *R3c* symmetry possesses G-type antiferromagnetic order. Our calculations however did not consider possible site disorder among the Fe^{3+} and Ga^{3+} ions, commonly observed in the bulk gallium ferrite.[50] Experimental magnetization *versus* temperature measurement with a small probing field shows a weak magnetic response possibly suggesting AFM-order (please see the ESI†). The stability of the *R3c* phase was further evaluated by calculation of the phonon spectra, where no negative frequencies were observed bolstering the stability of the current phase under experimental conditions (please refer to the ESI†). Further electronic structure calculations were carried out within the antiferromagnetic configurations of the Fe-spins without further consideration of specific antiferromagnetic order. Fig. 4(a) plots the electronic band structure, total and site projected density of states computed using GGA. It is observed that the material demonstrates direct bandgap characteristics albeit a much smaller bandgap (E_g ~0.5 eV) than that observed in our experimental study reported above. Such underestimation of the electronic bandgap within DFT studies using GGA is very common due to localized electronic states.[51,52] However, the band structure and site projected density of states computed here are good to describe the electronic structure in a qualitative manner. It is observed that the top of the valence band is predominantly made up of O 2p states while the bottom of the conduction band is composed of Fe 3d electronic states. To further treat the localized states of the Fe ion, on-site Coulomb (Hubbard) potential (U = 2–4 eV) was applied, within the GGA+U technique. The optimization of the Hubbard potential was accomplished by computing the electronic bandgap and comparing the bandgap with that obtained from the experiment. It is found that U_{eff} = 4.0 eV results in an E_g ~2 eV, closely corresponding to the experimental observation. Furthermore, the qualitative description of the band structure and DOS remained similar with and without application of U_{eff}.

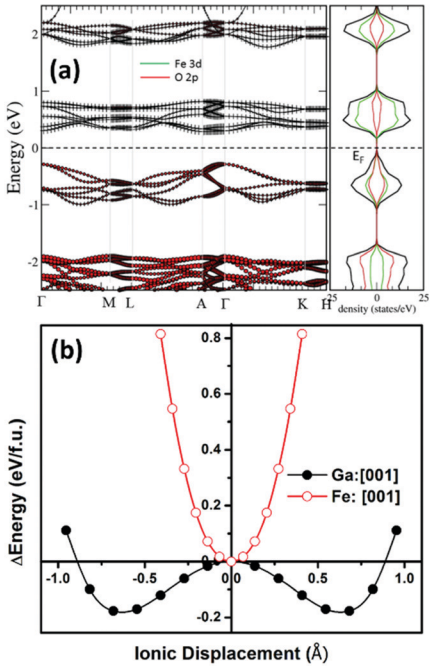

Fig. 4 (a) Electronic structure of *R3c*-GFO calculated using GGA. The figure in the left plots the band structure along the high symmetry directions. The right panel plots the total and angular momentum resolved density of states (DOS). (b) Energy landscape of *R3c*-GFO while it switches between the polar states *via* centrosymmetric phase demonstrating double-well, characteristic of ferroelectrics when Ga-ions are moved with respect to the surrounding O-ions, along the polar axis.

To unravel the possible ferroelectric character of the material within *R3c* symmetry, DFT calculations were performed towards finding possible equivalent energy states which is the signature of ferroelectricity. In typical ferroelectric materials, the equivalent low energy polar states are separated by a high energy state with higher symmetry and the transition path follows an energy double-well. The immediate higher symmetry super-group is $R\bar{3}c$ which has a close symmetry relation with the present *R3c* phase. In temperature-dependent dielectric measurements, we observed anomalies around ~525 K and 650 K, respectively, possibly indicating symmetry-increasing phase transformation. At this moment, we are not very sure whether the dielectric anomaly is due to $R3c \rightarrow R\bar{3}c$ transformation though this transformation is quite likely. The direction of spontaneous polarization of the *R3c*

structure within the hexagonal setting is [0001] *i.e.*, along the *c*-axis of the unit cell. The transition between the polar *R*3*c* states through the centrosymmetric $R\bar{3}c$ state takes place by means of coordinated displacements of the ions. Therefore, to compute a possible ferroelectric energy double-well, we transformed the structure with *R*3*c* symmetry to $R\bar{3}c$ using the utility program PSEUDO[53] within the Bilbao crystallographic server. In the process, the unit cell parameters were not symmetrized which may possibly contain some symmetry-breaking strain. With reference to the $R\bar{3}c$ symmetry, Ga^{3+} and Fe^{3+} ions were moved along the [0001] direction in both positive and negative senses and the corresponding total energy of the system was computed. Fig. 4(b) plots the total energy of the system with reference to the $R\bar{3}c$ phase, as it transforms to *R*3*c*. It is observed that while shifting of the Fe^{3+}-ion along the *c*-axis increases the total energy of the system monotonically, shifting the Ga^{3+}-ion along [0001] lowers the total energy of the system up to a minimum which corresponds to the *R*3*c* phase. Further shifting of the Ga^{3+}-ion, however, resulted in the increase of the total energy. Thus, *R*3*c*-GFO demonstrates an energy double-well when Ga^{3+}-ions are shifted along the direction of spontaneous polarization, [0001]. As mentioned earlier, this double-well formation of the polar crystal is the signature of the ferroelectricity in the system. Similar double-well formation was also demonstrated in the bulk orthorhombic $Pna2_1$ phase of GFO,[10] multiferroic bismuth ferrite (BFO)[54] with *R*3*c* symmetry and other prototype ferroelectrics.[55] While bulk GFO demonstrates requirement of large energy[10] vis-à-vis a large voltage for polarization switching[20] the present nanostructure with *R*3*c* symmetry requires much smaller energy, even smaller than that required by BFO with *R*3*c* symmetry[54] suggesting requirement of a small switching voltage. Furthermore, the contribution to the ferroelectricity in *R*3*c*-GFO is mainly from the Ga^{3+}-ions in contrast to the bulk phase where a systematic movement of the Fe^{3+}-ions had been demonstrated to result in the ferroelectric instability within the $Pna2_1$ phase. However, BFO with *R*3*c* symmetry demonstrates ferroelectricity originating from the Bi^{3+}-ions.

The magnitude of the spontaneous polarization was computed using the Berry phase method as described in the Modern theory of polarization.[34] In this method, the electronic contribution to the total polarization is described by the Berry phase. For GFO with *R*3*c* symmetry, Berry phase computation yields a polarization lattice, $6.05 + n \times 73.31\ \mu C\ cm^{-2}$ along [0001] direction, where n is an integer. In order to estimate the spontaneous polarization of the system, Berry phase calculation was further computed on the high symmetry $R\bar{3}c$ phase, $-15.34 + n \times 73.31\ \mu C\ cm^{-2}$ along the [0001] direction. The difference between the polarization of the above two phases yields the spontaneous polarization, P_s of the *R*3*c* phase, $21.39\ \mu C\ cm^{-2}$. The entire calculation was carried out within GGA. Application of U, within GGA+U with different U_{eff} values, resulted in P_s of 25.08, 23.12, and 24.01 $\mu C\ cm^{-2}$ for U_{eff} = 2, 3, and 4 eV, respectively. Estimated spontaneous polarization is markedly higher than the one obtained from the P–E loop in the previous section. This could be attributed to poor sample quality and defects in the sample. It is further observed that the electronic contribution to the total polarization in the system is comparable with the ionic contribution which potentially suggests a large shift current (related to the bulk photovoltaic effect) and thus promises the material's potential in novel photovoltaic applications. However, this aspect will be taken up in our follow-up work.

4. Conclusion

Hydrothermal synthesis under controlled processing conditions yields a novel, polar phase of gallium ferrite with rhombohedral *R*3*c* symmetry with unique geometry. Powder X-ray diffraction, Raman spectroscopy, and electron microscopy were employed to understand the phase evolution. It was argued that burst nucleation followed by diffusion controlled growth under high supersaturation resulted in the formation of the present phase with two different morphologies driven by the surface energies of different crystal surfaces. The optical absorption study reveals a moderate bandgap of $\sim$2.1 eV. Electrical measurement and scanning probe microscopy in conjunction with first-principles density functional theory based calculations demonstrated the signature of ferroelectricity. Berry phase calculation under modern theory of polarization showed a large contribution of electronic polarization to the spontaneous polarization of the material. This large electronic polarization together with a narrow bandgap would allow for novel optoelectronic and photovoltaic device designing.

Author contributions

M. M., P. S. S. S., and S. M. prepared samples and/or conducted characterization. A. R. did DFT calculations. S. M. and A. R. were responsible for data analyses, preparation, and revision of the manuscript. S. M., S. D., and A. R. were responsible for the overall supervision of the entire work.

Conflicts of interest

All authors have read and agreed to the published version of the manuscript.

Acknowledgements

A. R. thanks J. Bhagyaraj (IIT Kanpur) and Loknath Sathua (IIT Bhubaneswar), and D. Maurya (Virginia Tech.) for their help in electron microscopy. S. Mukherjee acknowledges DST for financial assistance (IFA13-MS-03) under the INSPIRE faculty award program to undertake this work. The work was supported by SERB, Govt. of India through project no. CRG/2019/003828.

References

1 J. F. Scott, *Science*, 2007, **315**, 954–959.
2 C. A. F. Vaz, Y. J. Shin, M. Bibes, K. M. Rabe, F. J. Walker and C. H. Ahn, *Appl. Phys. Rev.*, 2021, **8**, 41308.
3 G. Hodes, *Science*, 2013, **342**, 317–318.

4 M. D. McGehee, *Nat. Mater.*, 2014, **13**, 845–846.
5 M. Antonietta Loi and J. C. Hummelen, *Nat. Mater.*, 2013, **12**, 1087.
6 Q. Wang and A. Abate, *Adv. Mater. Interfaces*, 2018, **5**, 1800264.
7 C. N. R. Rao, *Annu. Rev. Phys. Chem.*, 1989, **40**, 291–326.
8 R. Nechache, C. Harnagea, S. Li, L. Cardenas, W. Huang, J. Chakrabartty and F. Rosei, *Nat. Photonics*, 2014, **9**, 61.
9 W. S. Choi, M. F. Chisholm, D. J. Singh, T. Choi, G. E. Jellison Jr. and H. N. Lee, *Nat. Commun.*, 2012, **3**, 689.
10 S. Mukherjee, A. Roy, S. Auluck, R. Prasad, R. Gupta and A. Garg, *Phys. Rev. Lett.*, 2013, **111**, 087601.
11 H. An, J. Y. Han, B. Kim, J. Song, S. Y. Jeong, C. Franchini, C. W. Bark and S. Lee, *Sci. Rep.*, 2016, **6**, 28313.
12 I. Grinberg, D. V. West, M. Torres, G. Gou, D. M. Stein, L. Wu, G. Chen, E. M. Gallo, A. R. Akbashev, P. K. Davies, J. E. Spanier and A. M. Rappe, *Nature*, 2013, **503**, 509.
13 H. Matsuo, Y. Noguchi and M. Miyayama, *Nat. Commun.*, 2017, **8**, 207.
14 J. He, C. Franchini and J. M. Rondinelli, *Chem. Mater.*, 2017, **29**, 2445–2451.
15 G. Catalan and J. F. Scott, *Adv. Mater.*, 2009, **21**, 2463–2485.
16 M. M. Seyfouri and D. Wang, *Crit. Rev. Solid State Mater. Sci.*, 2020, 1–26.
17 S. M. Young, F. Zheng and A. M. Rappe, *Phys. Rev. Lett.*, 2012, **109**, 1–5.
18 M. Mishra, A. Roy, A. Garg, R. Gupta and S. Mukherjee, *J. Alloys Compd.*, 2017, **721**, 593–599.
19 S. Mukherjee, V. Ranjan, R. Gupta and A. Garg, *Solid State Commun.*, 2012, **152**, 1181–1185.
20 S. Song, H. M. Jang, N. S. Lee, J. Y. Son, R. Gupta, A. Garg, J. Ratanapreechachai and J. F. Scott, *NPG Asia Mater.*, 2016, **8**, e242–9.
21 V. Singh, K. Brajesh, S. Sahu, A. Garg and R. Gupta, *J. Am. Ceram. Soc.*, 2019, **102**, 7414–7427.
22 R. Arielly, W. M. Xu, E. Greenberg, G. K. Rozenberg, M. P. Pasternak, G. Garbarino, S. Clark and R. Jeanloz, *Phys. Rev. B: Condens. Matter Mater. Phys.*, 2011, **84**, 1–8.
23 M. Mishra, I. Mukherjee, A. K. Mall, A. Mitra, S. Dash, S. Chatterjee, S. Mukherjee and A. Roy, *J. Mater. Chem. A*, 2018, **6**, 13031–13040.
24 J. Rodríguez-Carvajal, *Phys. Rev. B: Condens. Matter Mater. Phys.*, 1993, **192**, 55–69.
25 R. O. Jones and O. Gunnarsson, *Rev. Mod. Phys.*, 1989, **61**, 689–746.
26 G. Kresse and J. Furthmüller, *Phys. Rev. B: Condens. Matter Mater. Phys.*, 1996, **54**, 11169–11186.
27 G. Kresse and D. Joubert, *Phys. Rev. B: Condens. Matter Mater. Phys.*, 1999, **59**, 1758–1775.
28 J. P. Perdew, K. Burke and Y. Wang, *Phys. Rev. B: Condens. Matter Mater. Phys.*, 1996, **54**, 16533–16539.
29 B. Himmetoglu, A. Floris, S. de Gironcoli and M. Cococcioni, *Int. J. Quantum Chem.*, 2014, **114**, 14–49.
30 S. A. Tolba, K. M. Gameel, B. A. Ali, H. A. Almossalami and N. K. Allam, *The DFT+U: Approaches, Accuracy, and Applications*, ed. G. Yang, IntechOpen, Rijeka, 2018, vol. 1.
31 S. L. Dudarev, G. A. Botton, S. Y. Savrasov, C. J. Humphreys and A. P. Sutton, *Phys. Rev. B: Condens. Matter Mater. Phys.*, 1998, **57**, 1505–1509.
32 W. Kohn and L. J. Sham, *Phys. Rev.*, 1965, **140**, A1133–A1138.
33 J. P. Perdew and Y. Wang, *Phys. Rev. B: Condens. Matter Mater. Phys.*, 1992, **45**, 13244–13249.
34 D. Vanderbilt, *Phys. Rev. B: Condens. Matter Mater. Phys.*, 1993, **47**, 1651–1654.
35 P. Hermet, M. Goffinet, J. Kreisel and P. Ghosez, *Phys. Rev. B: Condens. Matter Mater. Phys.*, 2007, **75**, 220102.
36 K. P. Rice, A. E. Saunders and M. P. Stoykovich, *J. Am. Chem. Soc.*, 2013, **135**, 6669–6676.
37 R. Buonsanti, V. Grillo, E. Carlino, C. Giannini, T. Kipp, R. Cingolani and P. D. Cozzoli, *J. Am. Chem. Soc.*, 2008, **130**, 11223–11233.
38 T.-D. Nguyen, C.-T. Dinh, D.-T. Nguyen and T.-O. Do, *J. Phys. Chem. C*, 2009, **113**, 18584–18595.
39 T.-D. Nguyen, *Nanoscale*, 2013, **5**, 9455–9482.
40 L. Z. Mezey, D. Marton and J. Giber, *Period. Polytech., Mech. Eng.*, 1977, **21**, 189–216.
41 C. Rottman and M. Wortis, *Phys. Rev. B: Condens. Matter Mater. Phys.*, 1981, **24**, 6274–6277.
42 X. Peng, *Adv. Mater.*, 2003, **15**, 459–463.
43 Y. Ogawa, Y. Kaneko, J. P. He, X. Z. Yu, T. Arima and Y. Tokura, *Phys. Rev. Lett.*, 2004, **92**, 47401.
44 J. Tauc and A. Menth, *J. Non-Cryst. Solids*, 1972, **8–10**, 569–585.
45 J.-H. Park, B.-K. Kim, J.-G. Park, I.-T. Kim, H.-J. Je, Y. Klm and S. J. Park, *Ferroelectrics*, 1999, **230**, 151–156.
46 M. M. Kumar, V. R. Palkar, K. Srinivas and S. V. Suryanarayana, *Appl. Phys. Lett.*, 2000, **76**, 2764–2766.
47 Z. H. Sun, Y. L. Zhou, S. Y. Dai, L. Z. Cao and Z. H. Chen, *Appl. Phys. A: Mater. Sci. Process.*, 2008, **91**, 97–100.
48 J. M. Vila-Fungueiriño, A. Gómez, J. Antoja-Lleonart, J. Gázquez, C. Magén, B. Noheda and A. Carretero-Genevrier, *Nanoscale*, 2018, **10**, 20155–20161.
49 R. O. Jones and O. Gunnarsson, *Rev. Mod. Phys.*, 1989, **61**, 689–746.
50 T. Arima, D. Higashiyama, Y. Kaneko, J. P. He, T. Goto, S. Miyasaka, T. Kimura, K. Oikawa, T. Kamiyama, R. Kumai and Y. Tokura, *Phys. Rev. B: Condens. Matter Mater. Phys.*, 2004, **70**, 64426.
51 J. P. Perdew, W. Yang, K. Burke, Z. Yang, E. K. U. Gross, M. Scheffler, G. E. Scuseria, T. M. Henderson, I. Y. Zhang, A. Ruzsinszky, H. Peng, J. Sun, E. Trushin and A. Görling, *Proc. Natl. Acad. Sci. U. S. A.*, 2017, **114**, 2801–2806.
52 H. Baltache, R. Khenata, M. Sahnoun, M. Driz, B. Abbar and B. Bouhafs, *Phys. Rev. B: Condens. Matter Mater. Phys.*, 2004, **344**, 334–342.
53 C. Capillas, E. S. Tasci, G. de la Flor, D. Orobengoa, J. M. Perez-Mato and M. I. Aroyo, *Z. Kristallogr.*, 2011, **226**, 186–196.
54 P. Singh, A. Roy, A. Garg and R. Prasad, *J. Appl. Phys.*, 2015, **117**, 184104.
55 R. E. Cohen, *Nature*, 1992, **358**, 136–138.